

# **Dendritic trafficking faces fundamental speed-precision tradeoffs**

**Alex H. Williams<sup>1,2,3,\*</sup>, Cian O'Donnell<sup>2,4</sup>, Terrence Sejnowski<sup>2,5</sup>, and Timothy O'Leary<sup>6,7,\*</sup>**

<sup>4</sup> <sup>1</sup>Department of Neurosciences, University of California, San Diego, La Jolla, CA 92093, USA

<sup>5</sup> Howard Hughes Medical Institute, Salk Institute for Biological Studies, La Jolla, CA 92037, USA

<sup>6</sup> Department of Neurobiology, Stanford University, Stanford, CA 94305, USA

<sup>7</sup> Department of Computer Science, University of Bristol, Woodland Road, Bristol, BS8 1UB, United Kingdom

<sup>8</sup> Division of Biological Sciences, University of California at San Diego, La Jolla, CA 92093, USA

<sup>9</sup> Volen Center and Biology Department, Brandeis University, Waltham, MA 02454, USA

<sup>10</sup> <sup>7</sup>Department of Engineering, University of Cambridge, Trumpington St, Cambridge, CB2 1PZ, United Kingdom

<sup>11</sup>\*Address correspondence to: ahwillia@stanford.edu, toleary@brandeis.edu

## **ABSTRACT**

Most neurons have complex morphologies with long processes and dynamic, nonuniform spatial expression patterns of subcellular organelles and macromolecules. It is thought that trafficking and delivery of this subcellular cargo depends on purely local signals, rather than a global addressing system. Yet it remains unclear how such a decentralized system performs in complex morphologies. We mathematically formalize a previously proposed “sushi belt” model of microtubule transport (Doyle and Kiebler, 2011) and show how arbitrarily complex spatial distributions of cargo can be achieved by local signaling mechanisms. We reveal that this model predicts an unavoidable and physiologically critical tradeoff between speed and precision of cargo delivery that can be tested experimentally. More sophisticated variants of the sushi belt model can provide both fast and precise transport; however, these require global tuning of trafficking kinetics, and their performance is fragile to changes in the required spatial distribution of cargo.

<sup>14</sup> **Keywords:** Microtubules, Active transport, Tagging hypothesis, Dendrites, Transport, Morphology

## **INTRODUCTION**

The axonal and dendritic trees of most neurons are stunningly complex. The logistical task of distributing biomolecular components within these morphologies is therefore considerable, especially for components that are synthesized in locations that are distal from their site of use. Although the molecular machinery responsible for active transport has been characterized in detail (Doyle and Kiebler, 2011; Buxbaum et al., 2014a; Hancock, 2014), there have been few attempts to understand how these mechanisms can be orchestrated to distribute cargo accurately and efficiently in realistic neuron morphologies.

Not all aspects of neurite metabolism depend on continual delivery of cargo from the soma. For example, some forms of long-term potentiation (LTP) use local protein synthesis and can function in isolated dendrites (Kang and Schuman, 1996; Aakalu et al., 2001; Vickers et al., 2005; Sutton and Schuman, 2006). Similarly, constitutive maintenance of cytoskeletal, membrane and signalling pathways is achieved in part by locally recycling

26 or synthesizing components (Park et al., 2004, 2006; Grant and Donaldson, 2009; Zheng et al., 2015). Nonetheless,  
27 many long-lasting forms of synaptic plasticity are known to depend on anterograde transport of mRNAs (Kandel,  
28 2001; Puthanveettil et al., 2008) and specific mRNAs are known to be selectively transported to regions of heightened  
29 synaptic activity (Steward et al., 1998; Steward and Worley, 2001; Moga et al., 2004) or to developing synaptic  
30 contacts (Lyles et al., 2006). These observations fit with the well-known synaptic tagging hypothesis (Frey and  
31 Morris, 1997, 1998; Redondo and Morris, 2011), which proposes that synapses produce a biochemical ‘tag’ that  
32 signals a requirement for synaptic building blocks as part of the plasticity process. More generally, any site or  
33 region of a dendrite that requires specific biochemical components presumably needs to signal demand for these  
34 components and sequester them as they are delivered.

35 Kinesin and dyenin motor proteins mediate transport along microtubules at rates that far exceed passive diffusion  
36 (Block et al., 1990; Smith and Simmons, 2001; Hirokawa et al., 2010; Gagnon and Mowry, 2011; Park et al., 2014).  
37 The movement of individual cargoes is often stochastic and bidirectional (Hancock, 2014), motivating the hypothesis  
38 that motor proteins search the dendritic tree for dropoff locations, instead of following a pre-determined path (Welte,  
39 2004; Bressloff and Newby, 2009; Doyle and Kiebler, 2011). Thus, the local rate of transport and the decision to  
40 release cargo are thought to be predominantly controlled by localized signaling pathways, rather than a centralized  
41 addressing system. These localized mechanisms are not fully understood, but are believed to involve transient  
42 elevations in second-messengers like  $[Ca^{2+}]$  and ADP (Mironov, 2007; Wang and Schwarz, 2009; Buxbaum et al.,  
43 2014b), and changes in microtubule-associate proteins (Soundararajan and Bullock, 2014). These pathways can be  
44 activated by the spatial pattern of synaptic activity, the spontaneous release of calcium from internal stores, or by  
45 released factors from other cells (Wong and Ghosh, 2002; Parrish et al., 2007; Park and Poo, 2013; Zagrebelsky and  
46 Korte, 2014).

47 Based on these observations, a number of reviews have advanced a conceptual model of molecular transport,  
48 in which cargo searches the dendritic arbor via a noisy walk before its eventual release or capture (Welte, 2004;  
49 Buxbaum et al., 2014a, 2015). Doyle and Kiebler (2011) refer to this as the “sushi belt model”. In this analogy,  
50 molecular cargoes are represented by sushi plates that are distributed on a conveyor belt, as is typical in certain  
51 restaurants. Customers sitting alongside the belt (representing specific locations or synapses along a dendrite) each  
52 have specific and potentially time-varying demands for the amount and type of sushi they consume, but they can  
53 only choose from nearby plates as they pass.

54 While the sushi belt model is intuitively plausible, a number of open questions remain. How can a trafficking  
55 system based on localized signals be engineered to accurately generate spatial distributions of cargo? How can  
56 two spatially separated regions of the neuron avoid interfering with each other, even though they can’t directly  
57 communicate? Within this family of models, are there multiple sets of trafficking parameters capable of producing  
58 the same distribution of cargo, and do they use qualitatively different strategies to produce it? Finally, how quickly  
59 and how accurately can cargo be delivered by this class of models, and do these measures of performance depend on  
60 morphology and the specific spatial pattern of demand?

61 Here, we formulate the sushi belt model in a minimal, biophysically plausible set of equations, and show that it  
62 can reliably produce complex spatial distributions of cargo. However, we also reveal several logistical constraints on  
63 this family of models. In particular, we show that fast cargo delivery is error-prone, in the sense that the amount  
64 of cargo delivered is disproportionate to the local demand for cargo. We outline experimental predictions to test  
65 whether this tradeoff is present in real neurons, or if more complex models beyond the sushi belt are required.

66 **RESULTS**

67 **Model description**

68 Transport along microtubules is mediated by kinesin and dynein motors, which are responsible for anterograde and  
69 retrograde transport, respectively (Hirokawa et al., 2010; Gagnon and Mowry, 2011). Cargo is often simultaneously  
70 bound to both forms of motor protein, resulting in stochastic back-and-forth movements with a net direction  
71 determined by the balance of opposing movements (Welte, 2004; Hancock, 2014; Buxbaum et al., 2014a) (Fig. 1A).

72 To obtain a general model that can accommodate variations in the biophysical details, we interpreted microtubule-  
73 based transport as a biased random walk along a one-dimensional cable (Bressloff, 2006; Bressloff and Newby,  
74 2009; Newby and Bressloff, 2010; Bressloff and Newby, 2013). For each time step (1 s), the cargo moves 1  $\mu\text{m}$   
75 forwards, 1  $\mu\text{m}$  backwards, or remains in the same place, each with different probabilities. These parameters  
76 produce a qualitative fit to a more detailed biophysical model (Muller et al., 2008). In the simplest model, the  
77 probabilities associated with each movement are fixed and independent across each time step, with the forward jump  
78 more probable than a reverse jump, leading to a biased random walk (Fig. 1B, top panel). Existing biophysical  
79 models of single-cargo transport include mechanisms for extended unidirectional runs Muller et al. (2008); Hancock  
80 (2014). To account for these runs, we made a second version of the model in which the movement probabilities  
81 at each time step depend on the previous position of the particle (see *Methods*); the resulting trajectories change  
82 direction less frequently, resulting in a larger variance in cargo position over time (Fig. 1B, bottom panel).

83 While the position of individual cargoes is highly stochastic and dependent on the specific sequence of micro-  
84 scopic steps, the net movement of a population of cargoes (Fig. 1C) is predictable. This is seen in Figure 1D, which  
85 shows the distribution of 1000 molecules over time with (top panel) and without (bottom panel) unidirectional runs.  
86 Thus, bulk trafficking of cargo can be modeled as a deterministic process, which we refer to as the “mass-action  
87 model” of transport. The model discretizes the dendritic tree into small compartments, and describes the transfer of  
88 cargo between neighboring compartments as reactions with first order kinetics. In a cable with  $N$  compartments, the  
89 mass-action model is (Fig. 1E):

$$u_1 \xrightleftharpoons[b_1]{a_1} u_2 \xrightleftharpoons[b_2]{a_2} u_3 \xrightleftharpoons[b_3]{a_3} \dots \xrightleftharpoons[b_{N-1}]{a_{N-1}} u_N \quad (1)$$

90 where  $u_i$  is the amount of cargo in each compartment, and  $a_i$  and  $b_i$  respectively denote local rate constants for  
91 anterograde and retrograde transport. For now, we assume that these rate constants are spatially homogeneous, since  
92 the stochastic movements of our single-particle simulations do not depend on position. In this case, the mass-action  
93 model maps onto the well-known drift-diffusion equation (Fig. 1E) that can be used to estimate plausible parameter  
94 ranges from experimental data. The drift and diffusion coefficients are respectively proportional to the rate of change  
95 of the mean and variance of the ensemble distribution (see *Methods*); thus, measurements of these two quantities on  
96 a specific stretch of dendrite provide local estimates of the trafficking parameters.

97 Figure 1F shows two mass-action models with 1  $\mu\text{m}$  compartments. The trafficking rate constants were chosen  
98 to reproduce the mean and variance of the ensemble simulations in figure 1D. This resulted in  $a \approx 0.42 \text{ s}^{-1}$  and  
99  $b \approx 0.17 \text{ s}^{-1}$  for the simulation without runs (top panel) and  $a \approx 0.79 \text{ s}^{-1}$  and  $b \approx 0.54 \text{ s}^{-1}$  with runs (bottom panel).  
100 These parameters produce mean particle velocities of 15  $\mu\text{m}$  per minute for both simulations, which is within the  
101 range of experimental observations for microtubule transport (Rogers and Gelfand, 1998; Dynes and Steward, 2007;  
102 Muller et al., 2008). The variances of the particle distributions grow at a rate of 35 and 80  $\mu\text{m}^2$  per minute for the  
103 top and bottom panel, respectively.

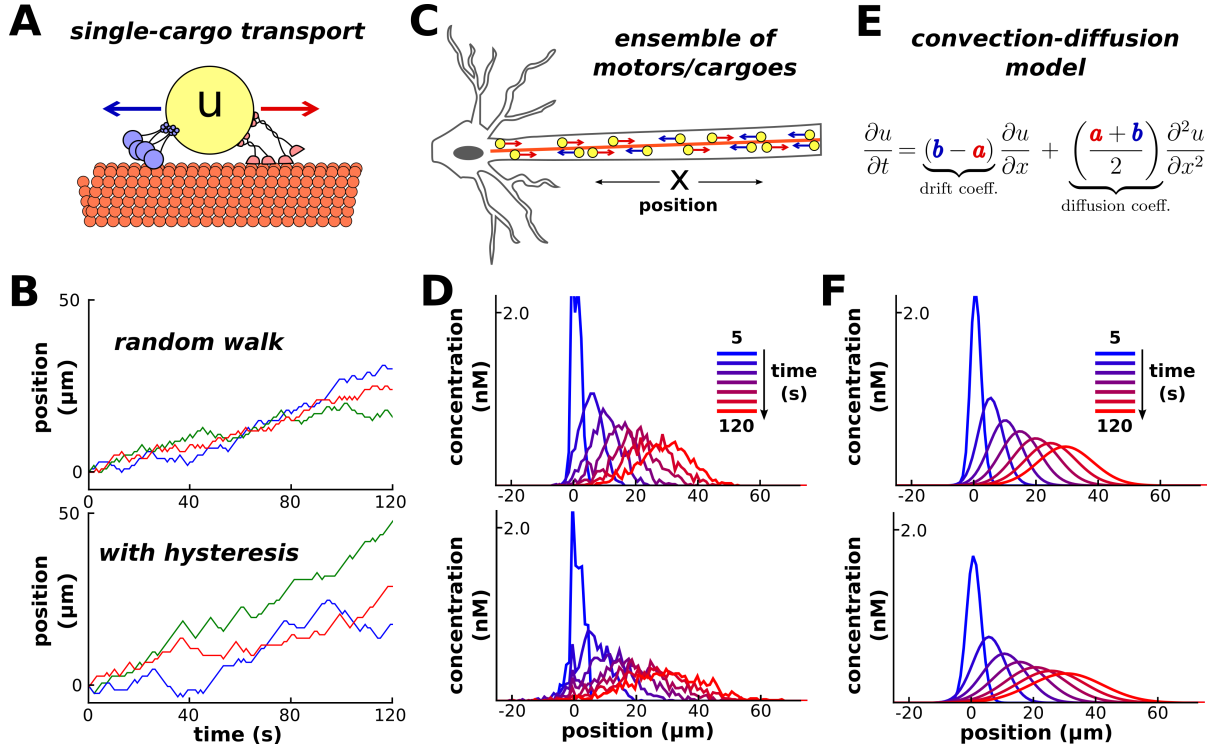


**Figure 1.** Model of microtubular transport. **(A)** Molecular cargo,  $u$ , undergoes stochastic back-and-forth movements driven by opposing motor proteins. **(B)** Three example random walks on a cable representing the movement of individual cargoes. In a simple random walk, each movement is independent of previous movements (top panel); longer unidirectional run result from adding history-dependence to the model, such that each movement is likely to continue in the same direction as the previous step (bottom panel). **(C)** An ensemble of synaptic cargoes transported along the length of a neurite. **(D)** The concentration profile of transported cargo along a cable over time, simulated as 1,000 independent random walks. Simulations with (bottom) and without (top) history-dependence. **(E)** In the limit of many individual particles, the concentration of  $u$  is described by a mass-action model (equation 1). The parameters  $a$  and  $b$  respectively scale the anterograde and retrograde rate of transport. **(F)** The mass-action model provides a good fit for the simulations in panel D.

The mass-action model is based on two important assumptions. First, we assumed that the net movement of molecules between neighboring compartments is a stochastic and memoryless process. This assumption is reasonable for cargoes that change direction often; specifically, on a length scale comparable to the size of the compartments. This appears to be the case under many (Muller et al., 2008; Verbrugge et al., 2009), though not necessarily all (Dynes and Steward, 2007; Soundararajan and Bullock, 2014) circumstances. However, we observed that the mass-action model could still be well-fit to simulated data where this assumption was violated (Fig. 1F, lower panel). In fact, the mass-action model only breaks down in the limit of very large run lengths (i.e. unidirectional, non-stochastic transport; see *Methods*).

The second assumption of the mass-action model is that there are many transported particles distributed throughout the dendritic tree. Many types of dendritic cargo are present in high numbers (Cajigas et al., 2012), and a deterministic model can provide a good approximation in this regime (Fig. 1D). The model also provides insight into the stochastic dynamics of transport for cargoes with fewer copy numbers. Instead of interpreting  $u$  as the amount of cargo in each compartment, this variable (when appropriately normalized) can be interpreted as

117 the probability that a single particle lies within a particular compartment. Thus, for a small number of transported  
118 cargoes, the mass-action model describes the average, or expected, distribution of the ensemble, with noise inversely  
119 proportional to the square root of the number of copies of cargo (see *Methods*).

## 120 A simple transport mechanism distributes cargo according to demand

121 We used the mass-action model for our simulations because it is easy to extend it to branched morphologies (Fig.  
122 2A), and to cases where the trafficking rate constants ( $a_i$  and  $b_i$ ) are spatially non-uniform. This situation corresponds  
123 to the kinetics of motor proteins being dependent on local biochemical signals (Mironov, 2007; Wang and Schwarz,  
124 2009; Soundararajan and Bullock, 2014).

125 In the model, the exchange of cargo between compartments approaches a steady-state ( $ss$ ), distribution over time  
126 (see *Methods*). The steady-state occurs when no net movement of cargo occurs between connected compartments.  
127 Mathematically, this occurs when:

$$\frac{u_p}{u_c} \Big|_{ss} = \frac{b}{a} \quad (2)$$

128 where  $u_p$  is the level in the “parent” compartment (closer to soma) and  $u_c$  is the level in the “child” compartment  
129 (closer to periphery);  $b$  and  $a$  refer to the trafficking rate constants between this pair of compartments.

130 Intuitively, in the mass-action model, the rate of cargo transfer is proportional to the concentration of cargo  
131 and the trafficking rate constant. Thus, the flow of cargo is equal and opposite when the ratio of cargo matches the  
132 reciprocal ratio of the rate constants between a pair of connected compartments.

133 The above result means that a specific spatial distribution of cargo can be achieved at steady state by modulating  
134 local trafficking rates. We denote the steady-state level of cargo in each compartment by  $\tilde{u}$  (we will soon show how  
135 this quantity can be encoded by a localized biochemical signal). If we interpret the steady state as being a specific  
136 “target concentration” (determined by local demand), we see that the ratio of local trafficking rates must satisfy:

$$\frac{b}{a} = \frac{\tilde{u}_p}{\tilde{u}_c} \quad (3)$$

137 For example, we produced a linear expression gradient (Magee, 1998; Hoffman et al., 1997) by setting  $\tilde{u}$  directly  
138 proportional to the distance from the soma. The trafficking rate constants in this case satisfy  $b_i/a_i = i/i + 1$  (where  $i$   
139 indexes on increasing distance to the soma). Figure 2B-C shows that this rule produced the expected profile, with  
140 the slope of the linear gradient controlled by tuning the total amount of cargo in the cable (Fig. 2C).

141 Together, this analysis shows that by manipulating local trafficking rates, arbitrary distributions of cargo can  
142 be achieved over time. We next incorporated a biologically plausible mechanism for controlling these rates. It is  
143 reasonable to assume that local trafficking rates can be modulated by a biochemical signal resulting from synaptic  
144 activation or local release of a growth factor. An experimentally characterized signal is provided by transient  
145 fluctuations in cytoplasmic calcium concentration,  $[Ca]_i$ , because increases in  $[Ca]_i$  are known to simultaneously  
146 arrest anterograde and retrograde microtubular transport for certain cargoes (Wang and Schwarz, 2009). We therefore  
147 assume, for any pair of compartments, the anterograde rate constant is determined by calcium concentration in the  
148 parent compartment,  $a = f([Ca]_p)$ , and the retrograde rate constant is determined by calcium concentration in the  
149 child compartment,  $b = f([Ca]_c)$ , where  $f$  is a function that describes how calcium concentration alters the transport

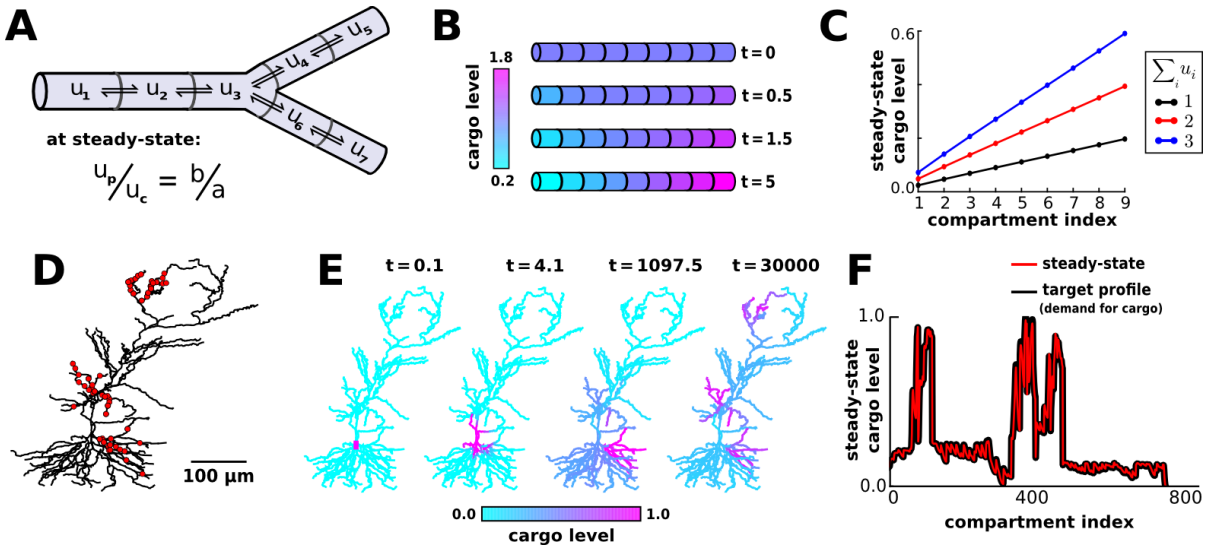


**Figure 2.** Local trafficking parameters determine the spatial distribution of biomolecules by a simple rule. (A) Diagram of the mass action transport model for a simple branched morphology. (B) A simulation of a nine compartment cable, with trafficking rate constants set to produce a linear gradient using the steady-state relation shown in panel A. (C) The slope of the linear gradient shown in panel B is directly proportional to the total amount of cargo in the model ( $\sum u_i$ ); the slope increases with increasing cargo levels, but the linear profile is preserved. (D) A model of a CA1 pyramidal cell with 742 compartments adapted from Migliore and Migliore (2012); excitatory synapses were added at the locations marked by red dots. (E) The average membrane potential in each compartment of the CA1 model determined  $\tilde{u}$ , which was used to determine values for the trafficking rate constants by equation (3). Over time, the spatial distribution of cargo evolved to match local demand. (F) The steady-state profile of cargo for each compartment in the simulation shown in panel E is precisely matched to local demand.

150 rates. This results in:

$$\frac{b}{a} = \frac{f([Ca]_c)}{f([Ca]_p)} = \frac{\tilde{u}_p}{\tilde{u}_c} \quad (4)$$

151 where  $\tilde{u}_i = 1/f([Ca]_i)$ .

152 Thus, in principle, local calcium transients that serve to arrest transport could provide a mechanism for  
 153 distributing cargo to an arbitrary target profile. We note that other potential signalling pathways could achieve the  
 154 same effect, so while there is direct evidence that  $[Ca]$  as a key signal, the model can be interpreted broadly, with  
 155  $[Ca]_i$  serving as a placeholder for any local signal identified experimentally. To test the global behavior of this model  
 156 in a complex morphology, we extended an existing multi-compartment model of a CA1 pyramidal neuron (Migliore  
 157 and Migliore, 2012). Excitatory synaptic input was delivered to 120 locations within three dendritic regions (red  
 158 dots, Fig. 2D), and the average membrane potential in each electrical compartment determined the target level  
 159 ( $\tilde{u}_i$ ) in each compartment (Methods). This models how molecular cargo could be selectively trafficked to active  
 160 synaptic sites (Fig. 2E, Supp. Video 1). Figure 2F confirms that the spatial distribution of  $u$  approaches the desired  
 161 steady-state exactly in the absence of noise.

## 162 Convergence rate

163 Biochemical processes are time-sensitive. For example, newly synthesized proteins must be delivered to synapses  
 164 within ~1 hour to support long-term potentiation in CA1 pyramidal cells (Frey and Morris, 1997, 1998; Redondo

and Morris, 2011). More generally, biochemical components whose abundance and localization are regulated by cellular feedback signals need to be distributed within a time interval that keeps pace with demand, within reasonable bounds. We therefore examined how quickly the spatial pattern of cargo converged to its target distribution.

In equations (3) and (4), we implicitly required each  $\tilde{u}_i > 0$  in order to avoid division by zero. Intuitively, if  $\tilde{u}_i = 0$  for some compartment, then no cargo can flow through that compartment, cutting off more peripheral compartments from the transport system. Similarly, if certain  $\tilde{u}_i$  are nearly equal to zero, then transport through these compartments will act as a bottleneck for transport, and convergence to the desired distribution will be slow.

Figure 3A-C illustrates and analyzes a bottleneck in a simple three compartment model. The two compartments on the end of the cable have the same desired level,  $\tilde{u}_1 = \tilde{u}_3$ ; the middle compartment acts as a bottleneck when  $\tilde{u}_2$  is very small (Fig. 3A). We can achieve this distribution with a simple mass-action model with only one free parameter,  $\varepsilon$ , which is the rate constant of trafficking into the middle compartment from either end; we fix the rate constant of trafficking out of the middle compartment to be 1 without loss of generality:

$$u_1 \xrightleftharpoons[1]{\varepsilon} u_2 \xrightleftharpoons[\varepsilon]{1} u_3 \quad (5)$$

We assume that  $u$  begins at one end of the cable, and examine the how taking  $\varepsilon$  to zero affects the convergence rate. Figure 3B shows that the convergence rate slows dramatically as  $\varepsilon$  decreases. The convergence rate is determined by the smallest magnitude, non-zero eigenvalue of the system (see Methods), which can be thought of as a rate-limiting step or process for the system. Simulations confirmed this analysis and showed that the convergence rate diverges to infinity as  $\varepsilon$  approaches zero (Fig. 3C).

We then asked whether the intuition from this three-compartment model extended to a cell with realistic morphology. We obtained qualitatively similar results. The CA1 model converged to a uniform target distribution more quickly than to a “bottleneck” target distribution, in which the middle third of the apical dendrite had low steady-state levels of cargo (Fig. 3D). Each pair of anterograde and retrograde rate constants was normalized to sum to one; thus, differences in convergence were not due to the scale of the trafficking rate constants.

In addition to this global view of convergence (Fig. 3D), we considered how the transport bottleneck affected transport to individual dendritic compartments. Consider a scenario where transported cargo produces a local chemical reaction after a certain quantity of cargo accumulates; for example, a recently potentiated synapse might be stabilized after enough plasticity-related factors are delivered from the soma. Figure 3E plots the duration of time it took for  $u_i$  to reach a pre-defined threshold for each compartment as a measure of the local transport delay. As expected, introducing a bottleneck caused much longer delays to compartments distal to that bottleneck (Fig. 3E, upper right portion of plot). The presence of a bottleneck *shortens* the transport delay to proximal compartments, compared to the uniform target distribution (Fig. 3E, lower left portion of plot). This occurs because cargo delayed by the bottleneck spreads throughout the proximal compartments, reaching higher levels earlier in the simulation. We observed qualitatively similar results for different local threshold values (data not shown).

The model predicts that transport to distal compartments will converge to steady-state at a faster rate when the steady-state level of cargo in the proximal compartments increases (Fig. 3D-E). This might be experimentally tested by measuring the convergence time of a retrogradely transported molecule that aggregates at recently activated synapses, such as *Arc* mRNA (Steward et al. (1998), see discussion). To illustrate this in the model CA1 cell, we characterized the time course of transport to the distal apical dendrite (stimulating stratum lacunosum/moleculare), proximal apical dendrite (stimulating stratum radiatum), entire apical dendrite (stimulating both layers), and entire

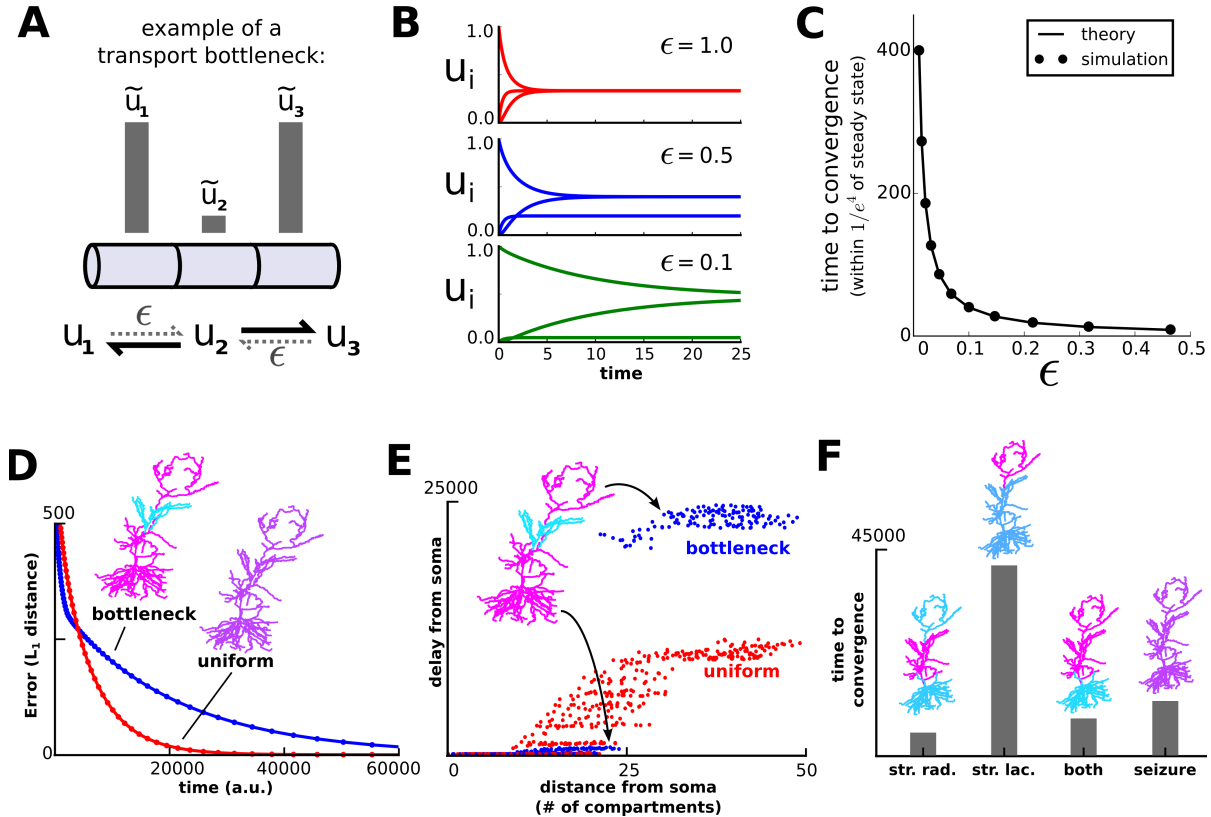


**Figure 3.** Convergence to steady-state is slow when molecules must be transported across bottlenecks—compartments with low target levels. **(A)** A three-compartment transport model, with the middle compartment acting as a bottleneck. The vertical bars represent the desired steady-state level of cargo in each compartment. The rate of transport into the middle compartment is small ( $\epsilon$ , dashed harpoons) relative to transport out of the middle compartment. **(B)** As  $\epsilon$  decreases, the model converges more slowly and the steady-state level decreases in the middle compartment. **(C)** Simulations (black dots) confirm that the time to convergence is given by the smallest non-zero eigenvalue of the system (analytically calculated line). This eigenvalue can be thought of as the rate-limiting step of the system. **(D)** Convergence ( $L_1$  distance) to a uniform target distribution (red line) is faster than a target distribution containing a bottleneck (blue line) in the CA1 model. **(E)** For all compartments that reach a threshold level ( $u_i = 0.001$ ), the simulated time it takes to reach threshold is plotted against the distance of that compartment to the soma. **(F)** Predicted convergence times for various target distributions (str. rad., stratum radiatum; str. lac., stratum lacunosum/moleculare) in the CA1 model.

203 cell (seizure). Notably, the model converges more slowly to distal input alone, than to paired distal and proximal  
204 input, or to an entirely uniform input distribution (Fig. 3F).

#### 205 **Microtubular trafficking, detachment and degradation on separated time scales**

206 We have so far considered how a target distribution of cargo can be generated by modulating the local rates  
207 of molecular motors. However, while certain types of molecular cargo stay on the microtubule network (e.g.  
208 mitochondria), many kinds of cargo must detach from the microtubules in order to be used at their final location. For  
209 example, dendritic mRNAs are transported along microtubules within densely-packed granules, and are released  
210 following granule disassembly (Krichevsky and Kosik, 2001; Buxbaum et al., 2014b). In this case, and in other  
211 cases where the cargo is disassembled or sequestered, it is reasonable to model detachment from the microtubule as

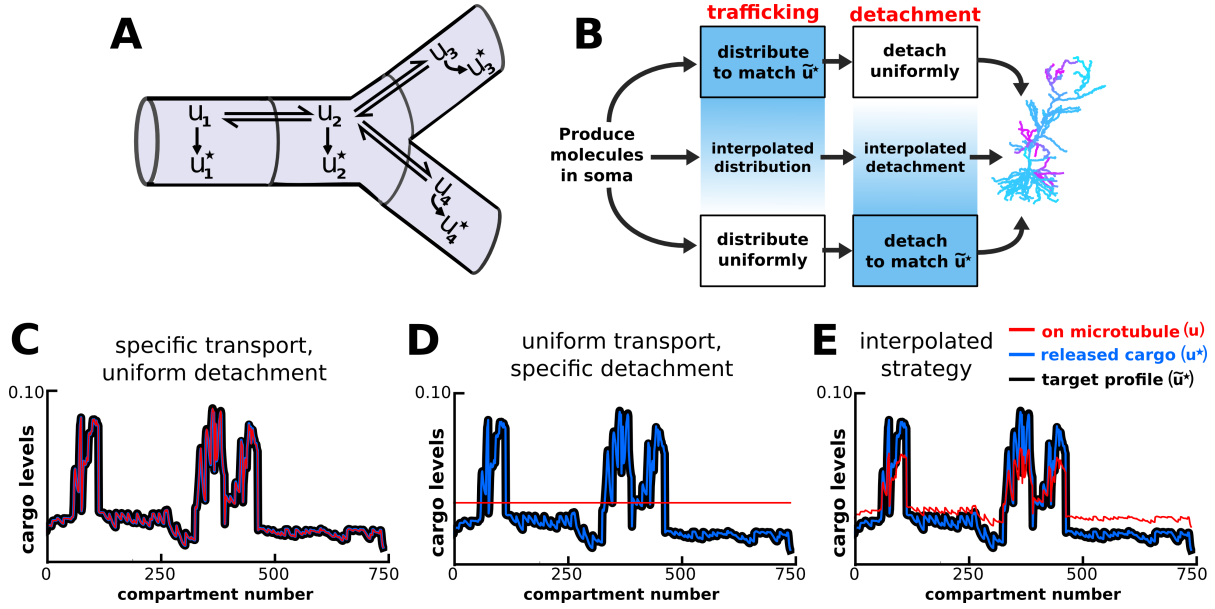
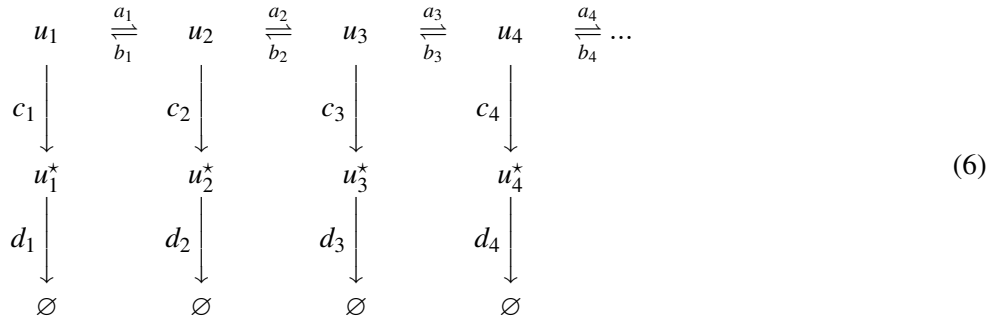


**Figure 4.** Multiple strategies for transport in a model including nonuniform microtubular detachment/activation. **(A)** Schematic of microtubular transport model with irreversible detachment in a branched morphology. The localized degradation reactions ( $u_i^* \xrightarrow{d_i} \emptyset$ ) are omitted for clarity. **(B)** Multiple strategies for producing a desired distribution of detached cargo ( $\tilde{u}^*$ ). When the timescale of detachment/delivery is sufficiently slow, the distribution of cargo on the microtubules approaches a quasi-steady-state (transport step). This known distribution can then be transformed into the desired distribution for  $\tilde{u}$  (detachment step). As long as these two steps are appropriately matched (blends of blue), then the desired distribution will be achieved (CA1 cell, right). **(C-E)** Quasi-steady-state distributions of  $u$  (red),  $u^*$  (blue), and  $\tilde{u}^*$  (black) for the various strategies diagrammed in panel B (see circled red numbers).

212 an irreversible process, followed by an eventual degradation.

213 This conceptual picture has been called the sushi belt model of transport (Doyle and Kiebler, 2011). This idea  
214 can be formalized as the following mass-action scheme:



215 As before, a molecule  $u$  is transported along a network of microtubules (top row, in equation 6). In each compartment,  
216 molecules can irreversibly detach from the microtubules in a reaction  $u_i \xrightarrow{c_i} u_i^*$ , where  $u^*$  denotes the biochemically  
217 active or released form of cargo. The final reaction,  $u_i^* \xrightarrow{d_i} \emptyset$ , models degradation in each compartment. Note that  
218 only  $u^*$  is subject to degradation; the molecule is assumed to be protected from degradation during transport. This  
219 model can be extended to branched morphologies (Fig. 3A).

220 To analyze this system we first assume that these three processes — trafficking, detachment, and degradation  
 221 — occur on separated timescales. If trafficking is sufficiently faster than detachment ( $a, b \gg c$ ), then  $u$  approaches  
 222 a quasi-steady state distribution defined by our previous analysis (equation 3). We then choose detachment rate  
 223 constants that transform the microtubular distribution into our desired distribution for  $u^*$ :

$$c_i \propto \frac{\tilde{u}_i^*}{\tilde{u}_i} \quad (7)$$

224 Here,  $\tilde{u}$  and  $\tilde{u}^*$  respectively denote the quasi-steady state distributions for  $u$  and  $u^*$ , respectively. As long as  
 225 degradation is sufficiently slow ( $c \gg d$ ) the desired distribution is transiently achieved.

226 The addition of spatially varied detachment rates ( $c_i$ ) produces a spectrum of strategies for achieving a desired  
 227 distribution of cargo (Fig. 4B). We can reproduce the essential strategy used in figure 2 by choosing the transport  
 228 rates ( $a_i, b_i$ ) to match the target distribution of cargo during the trafficking phase of transport (using equation 3).  
 229 Then, since the distribution is achieved at quasi-steady-state, the cargo can be detached uniformly ( $c_i = \text{constant}$ ,  
 230 with  $c \ll a, b$ ). Figure 4C shows simulated data confirming that the desired spatial distribution is first achieved along  
 231 the microtubules (red line, Fig. 4C) and then maintained after cargo is uniformly detached (blue line, Fig. 4C).

232 A second strategy begins by choosing uniform transport rates ( $a_i = b_i$ ), which evenly distributes cargo throughout  
 233 the dendritic tree. The desired distribution is then achieved by locally delivering cargo at a rate proportional to the  
 234 desired level ( $c_i \propto \tilde{u}_i^*$ ; Fig 4D). Unlike the first solution, this strategy avoids the transport bottlenecks examined in  
 235 Figure 3, and can achieve target patterns with  $\tilde{u}^*$  equal to zero in certain compartments by setting  $c_i = 0$ .

236 We refer to the first strategy (Fig. 4C) as the *specific trafficking model*, because cargo is selectively transported  
 237 to target sites. We refer to the second strategy (Fig. 4D) as the *uniform trafficking model*, because cargo is uniformly  
 238 distributed throughout the dendrite. These two strategies represent extremes on a spectrum of possible models (Fig.  
 239 4B). Figure 4E shows the behavior of an intermediate model, whose parameters are a linear interpolation between  
 240 the extreme strategies shown in Figure 4C and 4D. Thus, effective trafficking systems can be described as a spectrum  
 241 of strategies that may be suited to different situations and purposes (see Discussion).

## 242 Non-specific cargo delivery occurs when trafficking and detachment occur on similar timescales

243 We have demonstrated possible strategies for neurons to achieve precise and flexible transport of cargo by assuming  
 244 that cargo detachment is sufficiently slow relative to trafficking. However, biological neurons are unlikely to require  
 245 perfect matching between demand and distribution of cargo and may therefore tolerate loss of precision in order  
 246 to speed up delivery globally. We therefore examined the consequences of relaxing the separation of time scales  
 247 between transport and detachment.

248 Returning to the model of Figure 4, we consider a scenario where distal synaptic inputs on the apical tuft are  
 249 stimulated (Fig. 5A). If the average detachment rate constants are sufficiently slow, then, as before, cargo is delivered  
 250 selectively to the stimulated region (Fig. 5A, left). If we increase the detachment rates by a uniformly scaling,  
 251 some cargo “leaks off” the microtubule path on its way to the distal synapses (Fig. 5A, right). We refer to this as a  
 252 “non-specific” delivery of cargo, since cargo is not selectively delivered to the stimulated sites. Thus, speeding up  
 253 detachment relative to transport improves the overall rate at which cargoes are delivered to synapses, but this comes  
 254 at the cost of decreased accuracy of delivery.

255 Tradeoff curves between the average detachment rate constant and the non-specificity of transport for this  
 256 stimulation pattern are shown in figure 5B. Importantly, this tradeoff exists for both trafficking strategies we

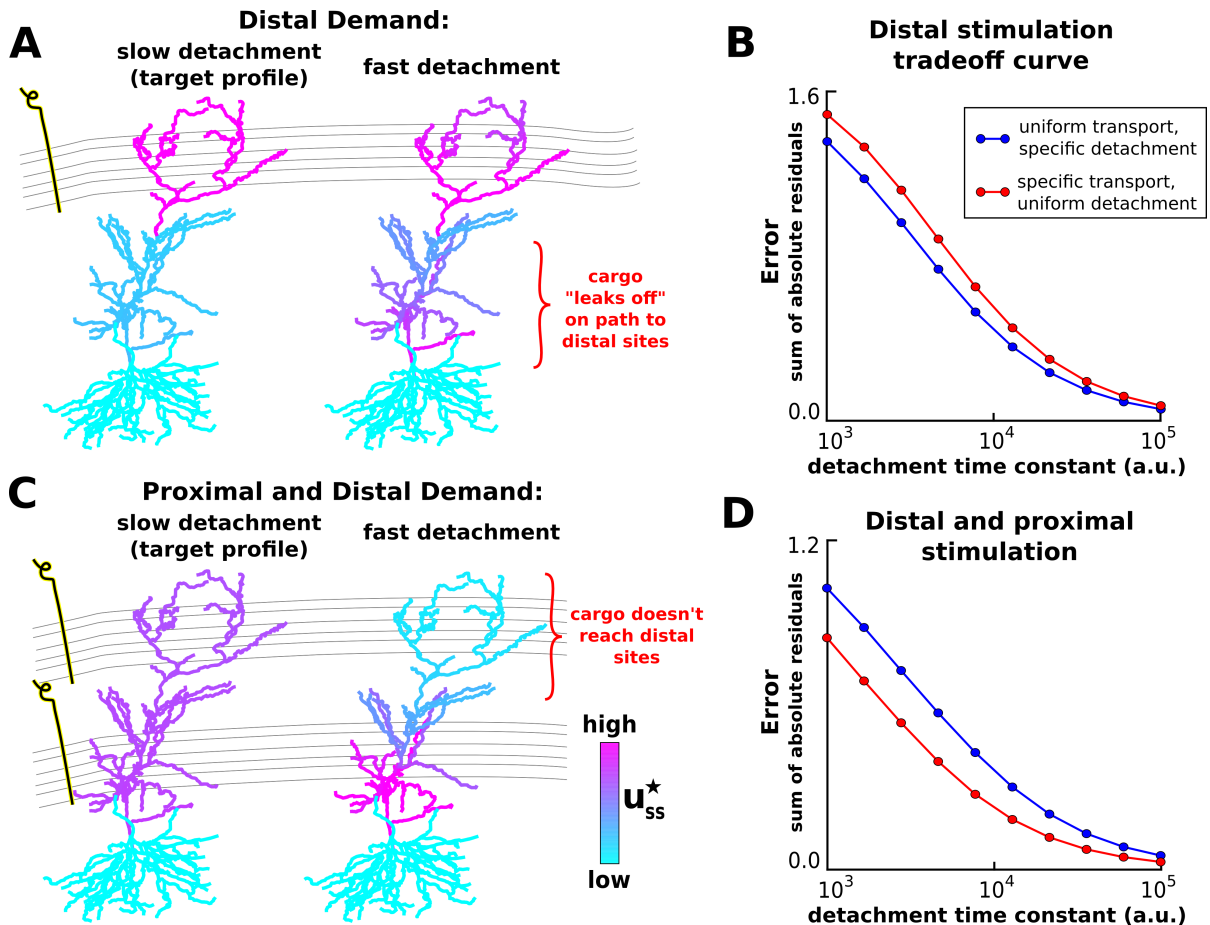


**Figure 5.** Proximal synapses capture more cargo at the expense of distal synapses when detachment rates are naïvely increased. (A) Delivery of cargo to the distal apical zone with slow (left) and fast detachment rates (right). The achieved pattern does not match the target distribution when detachment is fast, since some cargo is erroneously delivered to proximal sites. (B) Tradeoff curves between non-specificity and convergence rate for two trafficking strategies (blue line, see Fig 4D; red line, see Fig 4C). (C-D) Same as (A-B) but for intended cargo delivery to the entire apical tuft.

examined in figure 4 — the selective transport strategy (see Fig 4D) and uniform transport strategy (see Fig. 4C). For this stimulation pattern, the uniform trafficking strategy (Fig. 5B, blue line) outperforms the specific trafficking strategy (Fig. 5B, red line) since the latter suffers from bottleneck in the proximal apical zone.

The pattern of non-specific delivery is stimulation-dependent. When the entire apical tree is stimulated, fast detachment can result in a complete occlusion of cargo delivery to distal synaptic sites (Fig. 5C). As before, a tradeoff between specificity and delivery speed is present for both transport strategies (Fig. 5D). Interestingly, the specific trafficking strategy outperforms the uniform trafficking strategy in this case (in contrast to Fig. 5A-B). This is due to the lack of a bottleneck, and the fact that the uniform trafficking strategy initially sends cargo to the basal dendrites where it is not released.

Together, these results show that an increase in the efficiency of synaptic cargo delivery comes at the cost of loss of specificity and that the final destination of mis-trafficked cargo depends on the pattern of stimulation. We next asked whether we can tune the kinetic parameters of the transport mechanism to find an ideal compromise between

269 precision and trafficking efficiency.

## 270 **Transport speed and precision can be optimized for specific spatial patterns of demand**

271 In figure 5, we showed that scaling the detachment rates ( $c_i$ ), while leaving the transport rates ( $a_i, b_i$ ) fixed produces  
272 a proximal bias in cargo delivery. That is, synapses closer to the soma are more likely to capture cargo at the expense  
273 of distal synapses. We reasoned that increasing the anterograde transport rate of cargo could correct for this bias,  
274 producing transport rules that are both fast and precise.

275 We examined this possibility in a reduced model — an unbranched cable — so that we could develop simple  
276 heuristics that precisely achieve a desired distribution of cargo while minimizing the convergence time. In this  
277 model, cargo begins on the left end of the cable and is transported to a number of synaptic delivery sites, each of  
278 which is modeled as a double-exponential curve. We also restricted ourselves to investigating the uniform trafficking  
279 strategy (Fig. 4D); a similar analysis could in principle be done for the specific trafficking strategy.

280 As before, cargo can be precisely delivered to a variety of stimulation patterns when the detachment rate is  
281 sufficiently slow (Fig. 6A, Supp. Video 2); when the detachment rate is naïvely increased to speed up the rate of  
282 delivery, a proximal bias develops for all stimulation patterns (Fig. 6B, Supp. Video 3).

283 We then hand-tuned the transport rate constants to deliver equal cargo to six evenly spaced synaptic sites (top  
284 row of Fig. 6C, Supp. Video 4). Specifically, we increased the anterograde rate constants ( $a_i$ ) and decreased the  
285 retrograde rate constants ( $b_i$ ) by a decreasing linear function of position so that  $a_{N-1} = b_{N-1}$  at the right side of  
286 the cable. On the left end of the cable, we set  $a_1 = 0.5 + \beta$  and  $b_1 = 0.5 - \beta$ , where  $\beta$  is the parameter controlling  
287 anterograde bias. Intuitively, the profile of the proximal delivery bias is roughly exponential (Fig. 6B, top pattern),  
288 and therefore the anterograde rates need to be tuned more aggressively near the soma (where the bias is most  
289 pronounced), and more gently tuned as the distance to the soma increases.

290 However, this tuned model does not precisely deliver cargo for other stimulation patterns. For example, when  
291 the number of synapses on the cable is decreased, a distal delivery bias develops because too little cargo is released  
292 on the proximal portion of the cable (middle row, Fig. 6C; Supp. Video 5). Even when the number of synapses is  
293 held constant, changing the position of the synapses can disrupt equitable delivery of cargo to synapses. This is  
294 shown in the bottom row of figure 6C, where a distal bias again develops after the majority of activated synapses are  
295 positioned proximally. Thus, within the simple framework we've developed, the delivery of cargo can be tuned to  
296 achieve both precision and speed for a specified target distribution. However, non-specific cargo delivery occurs  
297 when different stimulation patterns are applied (assuming the transport parameters are not re-tuned).

## 298 **Conservative estimates of trafficking parameters suggest that the tradeoff between speed and 299 specificity is severe**

300 To examine these observations over a larger range of stimulation patterns and transport parameters, we plotted  
301 tradeoff curves between delivery precision and speed. We first examined a cable with six evenly spaced delivery  
302 sites (same as top row of Fig. 6A-C). As before, a hard tradeoff between specificity and delivery speed exists for the  
303 rationally designed model, which assumes separated time scales of transport and detachment (blue line in Fig. 6D).  
304 To get a rough estimate of how severe this tradeoff might be in real neurons, we set the length of the cable to 800  
305  $\mu\text{m}$  (roughly the length of an apical dendrite in a CA1 cell) and the diffusion coefficient to  $4 \mu\text{m}^2/\text{s}$  (an estimate  
306 on the upper end of what might be biologically achieved, see e.g. Caspi et al. (2000); Soundararajan and Bullock  
307 (2014)). Despite the optimistic estimate of the diffusion coefficient, the model predicts a severe tradeoff. It takes

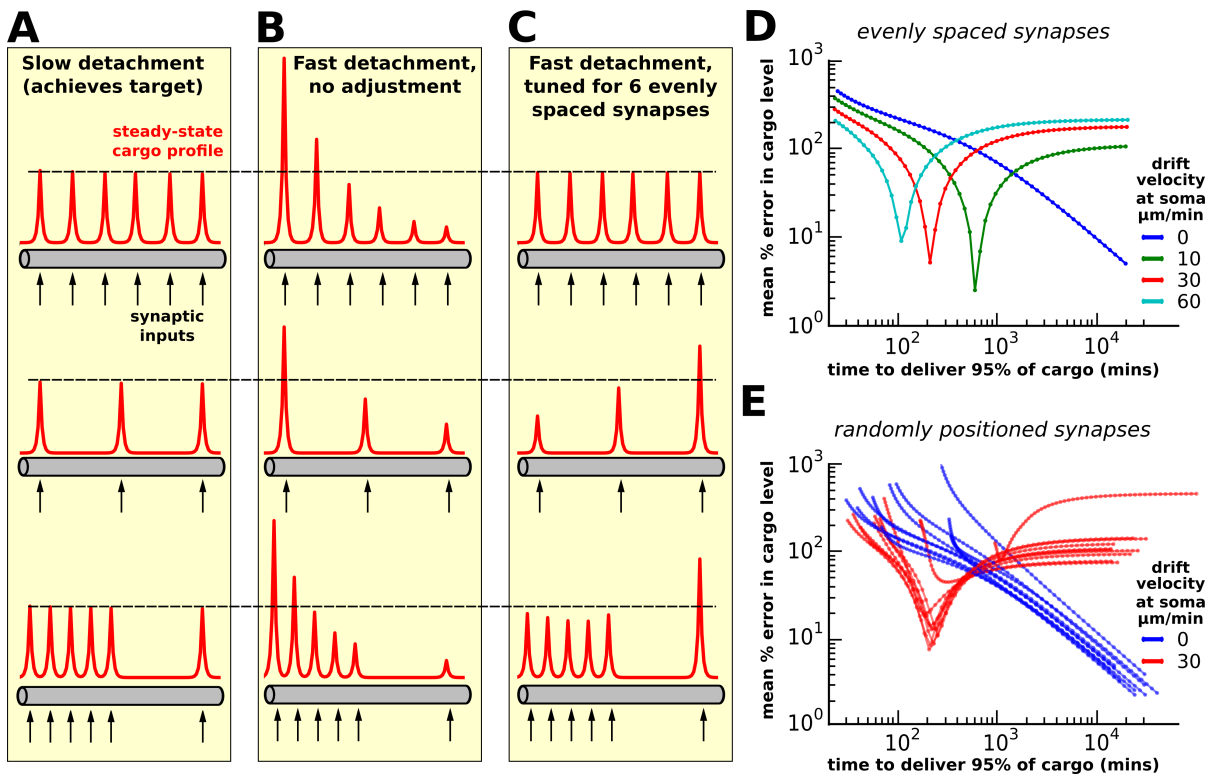


**Figure 6.** Tuning the model for speed and specificity is sensitive to the target distribution of cargo. (A-C) Cargo begins on the left end of an unbranched cable, and is ideally distributed equally amongst a number recently stimulated synaptic sites (black arrows). Steady-state cargo profiles (red) for three stimulation patterns (black arrows) along an unbranched cable. The dotted black line corresponds to the ‘target’ steady-state level at each delivery site. (A) When the timescale of detachment is sufficiently slow, cargo can be evenly distributed to the synapses regardless of their number and position. Transport parameters were set according to the procedure shown in figure 4D. (B) When detachment is naïvely increased (all rates multiplicatively scaled) a proximal bias in the steady-state distribution of cargo across all stimulation patterns. (C) Transport rate constants,  $a_i$  and  $b_i$ , were tuned to optimize the distribution of cargo to six equally spaced synapses (top row); detachment rate constants were the same as in panel B. Changing the number of synapses (middle row) or the position of the synapses (bottom row) causes the unequal distribution of cargo to synapses. (D) Tradeoff curves between non-specificity and convergence rate for six evenly spaced synapses (top row of A-C). Trafficking parameters were chosen so that the anterograde velocity decreased linearly over the length of the cable; the color of the lines shows the maximum velocity at the soma. The tradeoff curves shift to the left and becomes non-monotonic as the anterograde velocity increases. (E) Tradeoff curves for six randomly positioned synapses drawn uniformly across the cable. Ten simulations are shown for two levels of anterograde velocity (blue lines, 0  $\mu\text{m}/\text{min}$ ; red lines 30  $\mu\text{m}/\text{min}$ ); as before, the velocity linearly decreased across the length of the cable.

roughly 1 day to deliver cargo to match local demand with 10% average error, and roughly a week to deliver within 1% average error.

As the anterograde transport bias is introduced and increased (other line colors), the optimal points along the tradeoff curve move to the left, representing faster transport times. The tradeoff curves also become nonmonotonic: the error (non-specificity) initially decreases as the detachment rate decreases, but begins to increase after a certain well-matched point. Points on the descending left branch of the curve represent cargo distributions with proximal

314 bias (detachment is too fast); points on the ascending right branch correspond to distal bias (detachment is too slow).  
315 As suggested by the simulations shown in Fig. 6A-C, changing the pattern of cargo demand changes the tradeoff  
316 curves. Thus, we performed simulations to calculate tradeoff curves for randomizing the number (between 3 and  
317 9) and position of cargo demand hotspots (Fig. 6E). Notably, the untuned transport model (blue curves) always  
318 converge to zero error as the detachment rate decreases. In contrast, the model with anterograde bias (red curves)  
319 exhibit greater variability across demand patterns. Thus, for this model, it appears that the only way to achieve very  
320 precise, reliable and flexible transport is to have a slow detachment rate.

## 321 DISCUSSION

322 A microscope image of a typical dendritic tree hints at the complex logistical task that the neuron must solve in  
323 order to distribute its biomolecular components. While this problem is relevant to all aspects of cellular physiology  
324 in dendrites, synapses in particular are known to signal demand for specific kinds of molecules dynamically and can  
325 initiate distal metabolic events including transcription (Kandel, 2001; Deisseroth et al., 2003; Greer and Greenberg,  
326 2008; Ch'ng and Martin, 2011). This generates complex fluctuations in demand for specific kinds of molecular  
327 cargo that are involved in structural and physiological remodelling during plasticity and development. For example,  
328 excitatory synapses in the mammalian nervous system comprise hundreds of different proteins, including receptors,  
329 structural and anchoring proteins, and cytosolic signaling enzymes (Liu et al., 2014; Laßek et al., 2015). How do  
330 these components find their way to their final destination?

331 We formalized a well-known, parsimonious and plausible conceptual model of molecular transport, the sushi  
332 belt model (Doyle and Kiebler, 2011), to address this general question. We formulated this model as a simple  
333 mass-action system that has a direct biological interpretation and permits analysis and simulation. From this we  
334 developed a family of models based on the assumption that sequestration of cargo from a microtubule occurs on a  
335 slower timescale than trafficking along it. Intuitively, a consequence of this assumption is that the cargo has sufficient  
336 time to sample the dendritic tree for potential delivery sites (Welte, 2004). We showed that the same distribution  
337 of cargo could be achieved by a family of trafficking and release regimes: location-dependent trafficking followed  
338 by uniform release, uniform trafficking followed by location-dependent release, or a combination of these extreme  
339 cases (Fig. 4). Experimental findings appear to span these possibilities. Kim and Martin (2015) identified three  
340 mRNAs that were uniformly distributed throughout cultured *Aplysia* sensory neurons, but were targeted to synapses  
341 at the level of protein expression by localized translation. In contrast, the nonuniform expression of *Arc* mRNA  
342 is closely matched to the pattern of Arc protein in granule cells of the dentate gyrus (Steward et al., 1998; Farris  
343 et al., 2014; Steward et al., 2015). Even the same type of molecular cargo can show diverse movement statistics  
344 in single-particle tracking experiments (Dynes and Steward, 2007). Thus, our work places disparate experimental  
345 findings into a common conceptual framework and shows that a simple sushi belt model of transport can, in principle,  
346 maintain a specific distribution of cargo throughout a neuron and that this capacity is relatively independent of  
347 whether trafficking or cargo sequestration (or both) are controlled by local signals.

348 The model has a straightforward interpretation as a drift-diffusion process and the parameters describing drift  
349 rate and diffusion rate map directly to parameters in an equivalent mass-action scheme. This allowed us to estimate  
350 realistic rate parameters in the model from experimental data and then determine the consequences for distributing  
351 cargo throughout a typical dendritic arbor under a variety of assumptions and conditions. An inherent feature of the  
352 model is a trade-off between the rate at which cargo is distributed and the specificity, or accuracy with which its

353 distribution matches the spatial profile of demand.

354 We first asked whether the model could maintain precise delivery while relaxing the restriction of slow detachment  
355 relative to transport along a microtubule. We found that increasing the rate of detachment produces a proximal  
356 bias in the delivery of cargo, leading to a mismatch between supply and demand across a population of synapses.  
357 Intuitively, a fast microtubule detachment rate increases the chances for cargo to be delivered prematurely, without  
358 sufficiently searching for an appropriate delivery site.

359 When transport and sequestration are solely controlled by local signals the model predicts that the speed-  
360 specificity tradeoff is severe. In this version of the model, explored in Figures 4, 5 and 6, the timescale of cargo  
361 dissociation needs to be roughly an order of magnitude slower than the timescale of cargo distribution/trafficking.  
362 Thus, if it takes roughly 100 minutes to distribute cargo throughout the dendrites, it will take roughly 1000 minutes  
363 (~16-17 hours) before the cargo dissociates and is delivered to the synapses.

364 This unfavourable scaling has a number of implications. First, it might explain in part why local protein synthesis  
365 is observed in neurites across many species and neuron types. Long delays caused by microtubule transport from the  
366 soma would make rapid plasticity and metabolic responses impossible, severely limiting the regulatory capacity of  
367 neurons (Frey and Morris, 1997, 1998; Redondo and Morris, 2011). This may place fundamental limits on what can  
368 be achieved with synapse-to-nucleus signaling, which is widely thought to be an essential mechanism of neuronal  
369 plasticity. However, evidently not all dendritically expressed proteins are locally synthesized, and transcriptional  
370 blockade is known to interfere with regulation of synaptic and dendritic function (Nguyen et al., 1994; Bading,  
371 2000). This raises the question of whether delays for some kinds of proteins simply do not matter, or whether more  
372 sophisticated transport mechanisms might exist to mitigate delays.

373 We then asked whether the speed-specificity tradeoff could be circumvented by globally tuning basal anterograde  
374 and retrograde movement rates as a function of distance from the soma. Studies show that a directional bias in  
375 transport can be induced by changing the complement of motor proteins (Kanai et al., 2004; Amrute-Nayak and  
376 Bullock, 2012), and that such a change might be induced at the soma in response to synaptic activity (Puthanveettil  
377 et al., 2008). We were able to tune the transport rates to circumvent the speed-specificity tradeoff (Fig. 6C, top).  
378 Even when locations for cargo demand were uniformly placed across the cable, we found the trafficking rate  
379 constants needed to be tuned non-uniformly along a dendrite; in the cases we examined this could be achieved  
380 with a linearly decreasing profile (see *Methods*). However, biologically, it is unclear whether neurons are capable  
381 of globally tuning their trafficking rates in a non-uniform manner. Simply changing the composition of motor  
382 proteins (Amrute-Nayak and Bullock, 2012) is unlikely induce a spatial profile in transport bias. On the other  
383 hand, non-uniform modulation of the microtubule network or expression of microtubule-associated proteins provide  
384 potential mechanisms (Kwan et al., 2008; Soundararajan and Bullock, 2014), but this leaves open the question of  
385 how such non-uniform modifications arise to begin with. It would therefore be intriguing to experimentally test the  
386 existence of spatial gradients in anterograde movement bias, for example, using single-particle tracking in living  
387 neurons.

388 Furthermore, although tuning transport bias can provide fast and rapid cargo delivery for a specific arrangement  
389 of synapses along a dendrite, tuned solutions are very sensitive to changes in densities and spatial distributions  
390 of demand, as seen in Figure 6. This indicates that significant alterations in synaptic input or connectivity along  
391 a dendrite would preclude a tuned transport mechanism of this kind. In addition, the morphology of the neurites  
392 would affect the tuning, as introducing an anterograde bias can cause the accumulation of cargo at the tips of short

393 branches, proximal to the soma (data not shown). However, other mechanisms, not modeled in this study, might  
394 prevent this accumulation; for example, upon reaching the end of a neurite, a unit of cargo could undergo retrograde  
395 transport for long distances (Soundararajan and Bullock, 2014).

396 Certain neuron types may nonetheless have morphology and synaptic connectivity that is sufficiently stereotyped  
397 to allow transport mechanisms to be globally tuned to some degree. In these cases the qualitative prediction that  
398 anterograde bias should decrease as a function of distance to the soma can be tested experimentally. Such tuning,  
399 while providing improved efficiency in trafficking intracellular cargo, would also constitute a site of vulnerability  
400 because alterations in the kinetics of transport or the spatial distribution of demand easily lead to mismatch between  
401 supply and demand of cargo. Molecular transport is disrupted in a number of neurodegenerative disorders (Tang et al.,  
402 2012). One obvious potential explanation for this is that temporal delays in cargo distribution impair time-sensitive  
403 physiological processes. Our results highlight a less obvious kind of pathology: due to the broad requirement to  
404 appropriately match detachment and transport rates in the model, disruption of trafficking speed could additionally  
405 lead to spatially inaccurate cargo delivery. It would therefore be intriguing to examine whether pathologies caused  
406 by active transport defects are also associated with aberrant or ectopic localization of important cellular components.

407 What further experiments should be done to interrogate the model and test the predicted tradeoffs in speed,  
408 precision, and flexibility of transport? Our results suggest that the timescale of cargo dissociation from the  
409 microtubules is a critical parameter that merits careful examination. Local release of mRNA cargo can be induced  
410 by strong experimental manipulations, such as chemically-induced LTP and proteolytic digestion (Buxbaum et al.,  
411 2014a). Developing experimental tools that elicit more subtle effects on dissociation rate, as well as protocols to  
412 accurately observe and characterize dissociation in more naturalistic settings, would constrain the set of models we  
413 examined in this study. For example, our work predicts that decreasing the dissociation rate should produce minimal  
414 effects on the spatial distribution of cargo if dissociation occurs on a slower time scale than trafficking, whereas  
415 fine-tuned strategies (Fig. 6) are more sensitive to these manipulations.

416 It is possible that active transport in biological neurons will be more robust and flexible than our predictions,  
417 which are based on a simple, but widely invoked conceptual model. In particular, we modeled the dissociation of  
418 cargo from the microtubules as a single, irreversible chemical reaction. In reality, the capture of cargo may be more  
419 complex and involve regulated re-attachment. Similarly, the over-accumulation of cargo at a subset of synapses  
420 might be ameliorated if the dissociation process exhibited saturation or adaptation. Incorporating these details would  
421 change the behaviour of the model but would also need more detailed experiments to motivate them. Nonetheless,  
422 the minimal models we examined provide a basis for designing and interpreting future experiments, and serve as a  
423 rigorous exploration of an important and popular conceptual model.

## 424 METHODS

425 All simulation code is available on: <https://github.com/ahwillia/Williams-et-al-Synaptic-Transport>

### 426 Model of single-particle transport

427 Let  $x_n$  denote the position of a particle along a 1-dimensional cable at timestep  $n$ . Let  $v_n$  denote the velocity of  
428 the particle at timestep  $n$ ; for simplicity, we assume the velocity can take on three discrete values,  $v_n = \{-1, 0, 1\}$ ,  
429 corresponding to a retrograde movement, pause, or anterograde movement. As a result,  $x_n$  is constrained to take on  
430 integer values. In the memoryless transport model (top plots in Fig. 1B, 1D, and 1F), we assume that  $v_n$  is drawn

431 with fixed probabilities on each step. The update rule for position is:

$$x_{n+1} = x_n + v_n$$

432

$$v_{n+1} = \begin{cases} -1 & \text{with probability } p_- \\ 0 & \text{with probability } p_0 \\ 1 & \text{with probability } p_+ \end{cases}$$

433 We chose  $p_- = 0.2$ ,  $p_0 = 0.35$  and  $p_+ = 0.45$  for the illustration shown in Figure 1. For the model with  
 434 history-dependence (bottom plots in Fig. 1B, 1D, and 1F), the movement probabilities at each step depend on the  
 435 previous movement. For example, if the motor was moving in an anterograde direction on the previous timestep,  
 436 then it is more likely to continue to move in that direction in the next time step. In this case the update rule utilizes  
 437 *conditional* probabilities:

$$v_{n+1} = \begin{cases} -1 & \text{with probability } p(-|v_n) \\ 0 & \text{with probability } p(0|v_n) \\ 1 & \text{with probability } p(+|v_n) \end{cases}$$

438 In the extreme case of history-dependence, the particle always steps in the same direction as the previous time  
 439 step.

	$v_n = -1$	$v_n = 0$	$v_n = 1$
$p(v_{n+1} = -1)$	1	0	0
$p(v_{n+1} = 0)$	0	1	0
$p(v_{n+1} = 1)$	0	0	1

440 We introduce a parameter  $k \in [0, 1]$  to linearly interpolate between this extreme case and the memoryless model.  
 441 The bottom plots of figure 1B, 1D were simulated with  $k = 0.5$ ; in the bottom plot of figure 1F, a mass-action model  
 442 was fit to these simulations.

#### 443 Relationship of single-particle transport to the mass-action model

444 The mass-action model (equation 1, in the *Results*) simulates the bulk movement of cargo  $u$  across discrete  
 445 compartments. The rate of cargo transfer is modeled as elementary chemical reactions (Keener and Sneyd, 1998).  
 446 For an unbranched cable, the change in cargo in compartment  $i$  is given by:

$$\dot{u}_i = au_{i-1} + bu_{i+1} - (a+b)u_i \quad (8)$$

447 For now, we assume that the anterograde and retrograde trafficking rate constants ( $a$  and  $b$ , respectively) are spatially  
 448 uniform.

The mass-action model approximates the drift-diffusion partial differential equation (Fig. 1E) by discretizing  $u$  into spatial compartments. This can be seen by Taylor expanding around some position  $u(x)$ :

$$u(x) \approx a \left[ u(x) - \Delta \frac{\partial u}{\partial x} + \frac{\Delta^2}{2} \frac{\partial^2 u}{\partial x^2} \right] + b \left[ u(x) + \Delta \frac{\partial u}{\partial x} + \frac{\Delta^2}{2} \frac{\partial^2 u}{\partial x^2} \right] - (a+b) u(x) \quad (9)$$

$$= a \left[ -\Delta \frac{\partial u}{\partial x} + \frac{\Delta^2}{2} \frac{\partial^2 u}{\partial x^2} \right] + b \left[ \Delta \frac{\partial u}{\partial x} + \frac{\Delta^2}{2} \frac{\partial^2 u}{\partial x^2} \right] \quad (10)$$

449 where  $\Delta$  is the compartment size. We keep the first two terms of the Taylor expansion, due to the classic result that  
 450  $dx^2 \sim dt$  for a diffusion process (Gardiner, 2009). In the limit  $\Delta \rightarrow 0$ , we arrive at the drift-diffusion equation.

$$\dot{u}(x) = \frac{\partial u}{\partial t} = \underbrace{(b - a)}_{\text{drift coefficient}} \frac{\partial u}{\partial x} + \underbrace{\left(\frac{a+b}{2}\right)}_{\text{diffusion coefficient}} \frac{\partial^2 u}{\partial x^2}$$

451 When all cargo starts in one location (i.e. the initial condition is a delta function), then the distribution after some  
 452 elapsed time will be a Gaussian function. The mean of this Gaussian function changes in direct proportion to the  
 453 drift coefficient over time, while the variance is inversely proportional to the diffusion coefficient.

454 How does this equation relate to the model of single-particle transport (Fig. 1A-B)? For a memoryless biased  
 455 random walk, the expected position of a particle after  $n$  time steps is  $E[x_n] = n(p_+ - p_-)$  and the variance in position  
 456 after  $n$  steps is  $n(p_+ + p_- - (p_+ - p_-)^2)$ . For large numbers of independently moving particles (i.e. assuming  
 457 ergodicity), the ensemble of cargo will approach a Gaussian distribution by the Central Limit Theorem. This means  
 458 that the mean and variance calculations for a single particle can be directly related to the ensemble statistics outlined  
 459 in the previous paragraph. We find:

$$a = \frac{2p_+ - (p_+ - p_-)^2}{2}$$

460

$$b = \frac{2p_- - (p_+ - p_-)^2}{2}$$

461 The above analysis changes slightly when the single-particle trajectories contain long, unidirectional runs. The  
 462 expected position for any particle is the same  $E[x_n] = n(p_+ - p_-)$ ; the variance, in contrast, increases as run lengths  
 463 increase. However, the mass-action model can often provide a good fit in this regime with appropriately re-fit  
 464 parameters (see Fig. 1F). As long as the single-particles have stochastic and identically distributed behavior, the  
 465 ensemble will be well-described by a normal distribution by the central limit theorem. This only breaks down in the  
 466 limit of very long unidirectional runs, as the system is no longer stochastic.

## 467 Fitting local parameters of the mass-action model

468 The parameters of the mass-action model we study can be experimentally fit by estimating the drift and diffusion  
 469 coefficients of particles over the length of a neurite. A simple, and well-known, approach to doing this is to plot the  
 470 mean displacement and mean squared displacement of particles as a function of time. The slopes of the best-fit lines  
 471 in these cases respectively estimate the drift and diffusion coefficient. Diffusion might not accurately model particle  
 472 movements over short time scales, because unidirectional cargo runs result in superdiffusive motion, evidenced by  
 473 superlinear increases in mean squared-displacement (Caspi et al., 2000). Diffusion appropriately models particle  
 474 motion over longer time scales with stochastic changes in direction (Soundararajan and Bullock, 2014).

475 The mass-action model can also be fit by tracking the positions of a population of particles with photoactivatable  
 476 GFP (Roy et al., 2012). In this case, the distribution of fluorescence at each point in time could be fit by Gaussian  
 477 distributions; the drift and diffusion coefficients are respectively proportional to the rate at which the mean and  
 478 variance of this distribution changes.

479 **Steady-state analysis**

480 The steady-state ratio of trafficked cargo in neighboring compartments equals the ratio of trafficking rate constants  
 481 (equation 2). Consider a unbranched neurite with non-uniform anterograde and retrograde rate constants (equation  
 482 1). It is easy to verify the steady-state relationship in the first two compartments, by setting  $\dot{u}_1 = 0$  and solving:

$$-a_1 u_1 + b_1 u_2 = 0 \Rightarrow \frac{u_1}{u_2} \Big|_{ss} = \frac{b_1}{a_1}$$

483 Successively applying the same logic down the cable confirms the condition in equation 2 holds globally. A similar  
 484 procedure (starting at the tips and moving in) can be applied to branched morphologies to prove the more general  
 485 condition.

486 It is helpful to re-express the mass-action trafficking model as a matrix differential equation,  $\dot{\mathbf{u}} = A\mathbf{u}$ , where  
 487  $\mathbf{u} = [u_1, u_2, \dots, u_N]^T$  is the state vector, and  $A$  is the state-transition matrix. For a general branched morphology,  $A$  will  
 488 be nearly tridiagonal, with off-diagonal elements corresponding to branch points; matrices in this form are called  
 489 Hines matrices (Hines, 1984). For the simpler case of an unbranched cable,  $A$  is tridiagonal:

$$A = \begin{bmatrix} -a_1 & b_1 & 0 & & \dots & 0 \\ a_1 & -b_1 - a_2 & b_2 & 0 & & \\ 0 & a_2 & -b_2 - a_3 & b_3 & \ddots & \vdots \\ \vdots & 0 & a_3 & \ddots & & 0 \\ & & \ddots & -b_{N-2} - a_{N-1} & b_{N-1} & \\ 0 & & \dots & 0 & a_{N-1} & -b_{N-1} \end{bmatrix}$$

490 For both branched and unbranched morphologies, each column of  $A$  sums to zero, which reflects conservation of  
 491 mass within the system. The rank of  $A$  is exactly  $N - 1$  (this can be seen by taking the sum of the first  $N - 1$  rows,  
 492 which results in  $-1$  times the final row). Thus, the nullspace of  $A$  is one-dimensional (red lines in Supp. Fig. 1).

493 The desired steady-state distribution,  $\tilde{\mathbf{u}}$ , is an eigenvector that spans the nullspace of  $A$ . It is simple to show that  
 494 all other eigenvalues  $A$  are negative using the Gershgorin circle theorem; thus, the fixed point described by equation  
 495 2 is stable. The convergence rate is determined by the non-zero eigenvalue with smallest magnitude of  $A$ .

496 **CA1 pyramidal cell model**

497 We obtained a model published by Migliore and Migliore (2012) from the online repository ModelDB  
 498 (<https://senselab.med.yale.edu/modeldb/>), accession number 144541. We utilized this model to illustrate that our  
 499 analysis holds for complex, branched morphologies. Similar results can be achieved for different morphologies and  
 500 for different compartmental discretizations of the same morphology. We used the same spatial compartments used  
 501 by Migliore and Migliore (2012) and set the trafficking and dissociation parameters of the mass-action transport  
 502 model without reference to the geometry of the compartments. The mass-action model was simulated in Python; any  
 503 simulations of the electrical activity of the model (see Fig. 2) were performed using the Python API to NEURON  
 504 (Hines et al., 2009). We used a custom-written Python library to generate movies and figures for NEURON  
 505 simulations (Williams, 2016), which is available at: <https://github.com/ahwillia/PyNeuron-Toolbox>.

506 **Stochastic interpretation of the mass-action model**

507 The mass-action approximation holds in the limit of having a large number of transported particles. Cargoes with  
 508 small copy numbers (e.g. mitochondria) will operate in a stochastic regime. Intuitively, when each compartment  
 509 contains many particles, then small fluctuations in particle number don't appreciably change concentration. However,  
 510 these fluctuations can be functionally significant when the number of particles is small — for example, even a very  
 511 energetically favorable reaction cannot occur with zero particles, but may occur with reasonable probability when a  
 512 few particles are present.

513 The mass-action model nevertheless provides insight into these systems if we shift our perspective. Instead of  
 514 interpreting  $u_i$  as the amount of cargo in compartment  $i$ , we can interpret  $u_i$  as the *probability* of a particle occupying  
 515 compartment  $i$  at a particular time. This perspective evokes a standard technical assumption that the system is  
 516 *ergodic*, meaning that position of one particle averaged over very long time intervals is the same as the ensemble  
 517 steady-state distribution.

518 Thus, in addition to modeling how the spatial distribution of cargo changes over time, the mass-action model  
 519 equivalently models a spatial probability distribution. That is, imagine we track a single cargo and ask its position  
 520 after a long period of transport. The probability ratio between of finding this particle in any parent-child pair of  
 521 compartments converges to:

$$\left. \frac{p_p}{p_c} \right|_{ss} = \frac{b}{a}$$

522 which mirrors our steady-state analysis of the deterministic model.

523 In the stochastic model, the number of molecules in each compartment follows a binomial distribution at  
 524 steady-state; the coefficient of variation in each compartment is given by:

$$\sqrt{\frac{1 - p_i^{(ss)}}{n p_i^{(ss)}}}$$

525 This suggests that there are two ways of decreasing noise in the system. First, increasing the total number of  
 526 transported molecules,  $n$ , decreases the noise by a factor of  $1/\sqrt{n}$ . Additionally, transport is more reliable to  
 527 compartments with a high steady-state occupation probability.

528 **Incorporating detachment and degradation into the mass-action model**

529 Introducing detachment and degradation reactions into the transport model is straightforward. For an arbitrary  
 530 compartment in a cable, the differential equations become:

$$\begin{aligned}\dot{u}_i &= a_{i-1}u_{i-1} - (a_i + b_{i-1} + c_i)u_i + b_iu_{i+1} \\ \dot{u}_i^* &= c_iu_i - d_iu_i^*\end{aligned}$$

531 When  $a_i, b_i \gg c_i \gg d_i$ , then the variables  $u_i$  and  $u_i^*$  approach a quasi-steady-state, which we denote  $\tilde{u}_i$  and  $\tilde{u}_i^*$ .  
 532 For simplicity we assume  $d_i = 0$  in our simulations. We present two strategies for achieving a desired distribution  
 533 for  $\tilde{u}_i^*$  in figure 4C and 4D. To interpolate between these strategies, let  $F$  be a scalar between 0 and 1, and let  $\tilde{u}^*$  be  
 534 normalized to sum to one. We choose  $a_i$  and  $b_i$  to achieve:

$$\tilde{u}_i = F \tilde{u}_i^* + (1 - F)/N$$

535 along the microtubular network and choose  $c_i$  to satisfy

$$c_i \propto \frac{\tilde{u}_i^*}{F \tilde{u}_i^* + (1 - F)/N}$$

536 Here,  $N$  is the number of compartments in the model. Setting  $F = 1$  results in the simulation in the “specific”  
537 trafficking model (Fig. 4C), while setting  $F = 0$  results in the “uniform” trafficking model (Fig. 4D). An interpolated  
538 strategy is shown in figure 4E ( $F = 0.3$ ).

### 539 **Globally tuning transport rates to circumvent the speed-specificity tradeoff**

540 We investigated the *uniform trafficking model* with fast detachment rates in an unbranched cable with equally spaced  
541 synapses and  $N = 100$  compartments. Multiplicatively increasing the detachment rates across the cable produced a  
542 proximal bias in cargo delivery which could be corrected by setting the anterograde and retrograde trafficking rates  
543 to be:

$$a_i = 0.5 + \beta \cdot \frac{N - 1 - i}{N - 2}$$

$$b_i = 0.5 - \beta \cdot \frac{N - 1 - i}{N - 2}$$

544 where  $i = \{1, 2, \dots, N - 1\}$  indexes the trafficking rates from the soma ( $i = 1$ ) to the other end of the cable ( $i = N - 1$ ).  
545 Faster detachment rates require larger values for the parameter  $\beta$ ; note that  $\beta < 0.5$  is a constraint to prevent  $b_i$  from  
546 becoming negative. This heuristic qualitatively improved, but did not precisely correct for, fast detachment rates in  
547 the *specific trafficking model* (data not shown).

### 549 **ACKNOWLEDGEMENTS**

550 We thank Eve Marder and Benjamin Regner for useful feedback on the manuscript, and thank Simon Bullock for  
551 useful discussion. This research was supported by the Department of Energy Computational Science Graduate  
552 Fellowship, NIH Grant 1P01NS079419, NIH Grant P41GM103712, the Howard Hughes Medical Institute, and the  
553 Charles A. King Trust.

### 554 **COMPETING INTERESTS**

555 The authors declare that there are no competing interests.

### 556 **REFERENCES**

- 557 Aakalu, G., Smith, W. B., Nguyen, N., Jiang, C., and Schuman, E. M. (2001). Dynamic visualization of local protein  
558 synthesis in hippocampal neurons. *Neuron*, 30(2):489–502.
- 559 Amrute-Nayak, M. and Bullock, S. L. (2012). Single-molecule assays reveal that RNA localization signals regulate  
560 dynein-dynactin copy number on individual transcript cargoes. *Nat. Cell Biol.*, 14(4):416–423.
- 561 Bading, H. (2000). Transcription-dependent neuronal plasticity. *Eur. J. Biochem.*, 267(17):5280–5283.
- 562 Block, S. M., Goldstein, L. S. B., and Schnapp, B. J. (1990). Bead movement by single kinesin molecules studied  
563 with optical tweezers. *Nature*, 348(6299):348–352.
- 564 Bressloff, P. and Newby, J. (2009). Directed intermittent search for hidden targets. *New J. Phys.*, 11(2):023033.

- 565 Bressloff, P. C. (2006). Stochastic model of protein receptor trafficking prior to synaptogenesis. *Phys. Rev. E Stat. Nonlin. Soft. Matter. Phys.*, 74(3).
- 566 Bressloff, P. C. and Newby, J. M. (2013). Stochastic models of intracellular transport. *Rev. Mod. Phys.*, 85(1):135–196.
- 567 Buxbaum, A. R., Haimovich, G., and Singer, R. H. (2014a). In the right place at the right time: visualizing and  
568 understanding mRNA localization. *Nat. Rev. Mol. Cell Biol.*, 16(2):95–109.
- 569 Buxbaum, A. R., Wu, B., and Singer, R. H. (2014b). Single-Actin mRNA Detection in Neurons Reveals a Mechanism  
570 for Regulating Its Translatability. *Science*, 343(6169):419–422.
- 571 Buxbaum, A. R., Yoon, Y. J., Singer, R. H., and Park, H. Y. (2015). Single-molecule insights into mRNA dynamics  
572 in neurons. *Trends Cell Biol.*, 25(8):468–475.
- 573 Cajigas, I. J., Tushev, G., Will, T. J., tom Dieck, S., Fuerst, N., and Schuman, E. M. (2012). The local transcriptome  
574 in the synaptic neuropil revealed by deep sequencing and high-resolution imaging. *Neuron*, 74(3):453–466.
- 575 Caspi, A., Granek, R., and Elbaum, M. (2000). Enhanced diffusion in active intracellular transport. *Phys. Rev. Lett.*,  
576 85:5655–5658.
- 577 Ch’ng, T. and Martin, K. (2011). Synapse-to-nucleus signaling. *Curr. Opin. Neurobiol.*, 21:345–52.
- 578 Deisseroth, K., Mermelstein, P. G., Xia, H., and Tsien, R. W. (2003). Signaling from synapse to nucleus: the logic  
579 behind the mechanisms. *Curr. Opin. Neurobiol.*, 13(3):354–365.
- 580 Doyle, M. and Kiebler, M. A. (2011). Mechanisms of dendritic mRNA transport and its role in synaptic tagging.  
581 *EMBO J.*, 30(17):3540–3552.
- 582 Dynes, J. L. and Steward, O. (2007). Dynamics of bidirectional transport of Arc mRNA in neuronal dendrites. *J. Comp. Neurol.*, 500(3):433–447.
- 583 Farris, S., Lewandowski, G., Cox, C. D., and Steward, O. (2014). Selective Localization of Arc mRNA in Dendrites  
584 Involves Activity- and Translation-Dependent mRNA Degradation. *J. Neurosci.*, 34(13):4481–4493.
- 585 Frey, U. and Morris, R. (1998). Weak before strong: dissociating synaptic tagging and plasticity-factor accounts of  
586 late-LTP. *Neuropharmacol.*, 37(4-5):545–552.
- 587 Frey, U. and Morris, R. G. M. (1997). Synaptic tagging and long-term potentiation. *Nature*, 385(6616):533–536.
- 588 Gagnon, J. and Mowry, K. (2011). Molecular motors: directing traffic during RNA localization. *Crit Rev Biochem Mol Biol*, 46:229–39.
- 589 Gardiner, C. (2009). *Stochastic Methods: A Handbook for the Natural and Social Sciences (Springer Series in Synergetics)*. Springer, 4 edition.
- 590 Grant, B. D. and Donaldson, J. G. (2009). Pathways and mechanisms of endocytic recycling. *Nat. Rev. Mol. Cell Biol.*, 10(9):597–608.
- 591 Greer, P. L. and Greenberg, M. E. (2008). From synapse to nucleus: Calcium-dependent gene transcription in the  
592 control of synapse development and function. *Neuron*, 59(6):846 – 860.
- 593 Hancock, W. O. (2014). Bidirectional cargo transport: moving beyond tug of war. *Nat. Rev. Mol. Cell Biol.*,  
594 15(9):615–628.
- 595 Hines, M. (1984). Efficient computation of branched nerve equations. *Int. J. Biomed. Comput.*, 15(1):69–76.
- 596 Hines, M. L., Davison, A. P., and Muller, E. (2009). Neuron and python. *Front. Neuroinform.*, 3.
- 597 Hirokawa, N., Niwa, S., and Tanaka, Y. (2010). Molecular Motors in Neurons: Transport Mechanisms and Roles in  
598 Brain Function Development, and Disease. *Neuron*, 68(4):610–638.

- 605 Hoffman, D., Magee, J., Colbert, C., and Johnston, D. (1997). K<sup>+</sup> channel regulation of signal propagation in  
606 dendrites of hippocampal pyramidal neurons. *Nature*, 387:869–75.
- 607 Kanai, Y., Dohmae, N., and Hirokawa, N. (2004). Kinesin transports RNA: isolation and characterization of an  
608 RNA-transporting granule. *Neuron*, 43(4):513–525.
- 609 Kandel, E. R. (2001). The Molecular Biology of Memory Storage: A Dialogue Between Genes and Synapses.  
610 *Science*, 294(5544):1030–1038.
- 611 Kang, H. and Schuman, E. M. (1996). A requirement for local protein synthesis in neurotrophin-induced hippocampal  
612 synaptic plasticity. *Science*, 273(5280):1402–1406.
- 613 Keener, J. P. and Sneyd, J. (1998). *Mathematical Physiology*. Springer, New York.
- 614 Kim, S. and Martin, K. C. (2015). Neuron-wide RNA transport combines with netrin-mediated local translation to  
615 spatially regulate the synaptic proteome. *eLife*, 4:e04158.
- 616 Krichevsky, A. M. and Kosik, K. S. (2001). Neuronal RNA GranulesA Link between RNA Localization and  
617 Stimulation-Dependent Translation. *Neuron*, 32(4):683–696.
- 618 Kwan, A. C., Dombeck, D. A., and Webb, W. W. (2008). Polarized microtubule arrays in apical dendrites and axons.  
619 *Proc. Natl. Acad. Sci. U.S.A.*, 105(32):11370–11375.
- 620 Laßek, M., Weingarten, J., and Volknandt, W. (2015). The synaptic proteome. *Cell Tissue Res.*, 359(1):255–265.
- 621 Liu, X.-A., Kadakkuzha, B., Pascal, B., Steckler, C., Akhmedov, K., Yan, L., Chalmers, M., and Puthanveettil,  
622 S. V. (2014). New approach to capture and characterize synaptic proteome. *Proc. Natl. Acad. Sci. U.S.A.*,  
623 111(45):16154–16159.
- 624 Lyles, V., Zhao, Y., and Martin, K. C. (2006). Synapse Formation and mRNA Localization in Cultured Aplysia  
625 Neurons. *Neuron*, 49(3):349–356.
- 626 Magee, J. (1998). Dendritic hyperpolarization-activated currents modify the integrative properties of hippocampal  
627 CA1 pyramidal neurons. *J Neurosci*, 18:7613–24.
- 628 Migliore, M. and Migliore, R. (2012). Know your current I<sub>h</sub>: Interaction with a shunting current explains the  
629 puzzling effects of its pharmacological or pathological modulations. *PLoS ONE*, 7(5):e36867.
- 630 Mironov, S. L. (2007). ADP Regulates Movements of Mitochondria in Neurons. *Biophys. J.*, 92(8):2944–2952.
- 631 Moga, D., Calhoun, M., Chowdhury, A., Worley, P., Morrison, J., and Shapiro, M. (2004). Activity-regulated  
632 cytoskeletal-associated protein is localized to recently activated excitatory synapses. *Neurosci.*, 125(1):7–11.
- 633 Muller, M. J. I., Klumpp, S., and Lipowsky, R. (2008). Tug-of-war as a cooperative mechanism for bidirectional  
634 cargo transport by molecular motors. *Proc. Natl. Acad. Sci. U.S.A.*, 105(12):4609–4614.
- 635 Newby, J. and Bressloff, P. C. (2010). Local synaptic signaling enhances the stochastic transport of motor-driven  
636 cargo in neurons. *Phys. Biol.*, 7(3):036004.
- 637 Nguyen, P. V., Abel, T., and Kandel, E. R. (1994). Requirement of a critical period of transcription for induction of a  
638 late phase of ltp. *Science*, 265(5175):1104–1107.
- 639 Park, H. and Poo, M.-m. (2013). Neurotrophin regulation of neural circuit development and function. *Nat. Rev.  
640 Neurosci.*, 14(1):7–23.
- 641 Park, H. Y., Lim, H., Yoon, Y. J., Follenzi, A., Nwokafor, C., Lopez-Jones, M., Meng, X., and Singer, R. H. (2014).  
642 Visualization of dynamics of single endogenous mRNA labeled in live mouse. *Science*, 343(6169):422–424.
- 643 Park, M., Penick, E. C., Edwards, J. G., Kauer, J. A., and Ehlers, M. D. (2004). Recycling endosomes supply AMPA  
644 receptors for LTP. *Science*, 305(5692):1972–1975.

- 645 Park, M., Salgado, J. M., Ostroff, L., Helton, T. D., Robinson, C. G., Harris, K. M., and Ehlers, M. D. (2006).  
646 Plasticity-induced growth of dendritic spines by exocytic trafficking from recycling endosomes. *Neuron*, 52(5):817–  
647 830.
- 648 Parrish, J. Z., Emoto, K., Kim, M. D., and Jan, Y. N. (2007). Mechanisms that regulate establishment, maintenance,  
649 and remodeling of dendritic fields. *Annu. Rev. Neurosci.*, 30:399–423.
- 650 Puthanveettil, S. V., Monje, F. J., Miniaci, M. C., Choi, Y.-B., Karl, K. A., Khandros, E., Gawinowicz, M. A.,  
651 Sheetz, M. P., and Kandel, E. R. (2008). A New Component in Synaptic Plasticity: Upregulation of Kinesin in the  
652 Neurons of the Gill-Withdrawal Reflex. *Cell*, 135(5):960–973.
- 653 Redondo, R. L. and Morris, R. G. (2011). Making memories last: the synaptic tagging and capture hypothesis. *Nat. Rev. Neurosci.*, 12(1):17–30.
- 655 Rogers, S. L. and Gelfand, V. I. (1998). Myosin cooperates with microtubule motors during organelle transport in  
656 melanophores. *Curr. Biol.*, 8(3):161–164.
- 657 Roy, S., Yang, G., Tang, Y., and Scott, D. A. (2012). A simple photoactivation and image analysis module for  
658 visualizing and analyzing axonal transport with high temporal resolution. *Nat. Protoc.*, 7(1):62–68.
- 659 Smith, D. and Simmons, R. (2001). Models of Motor-Assisted Transport of Intracellular Particles. *Biophys. J.*,  
660 80(1):45–68.
- 661 Soundararajan, H. C. and Bullock, S. L. (2014). The influence of dynein processivity control, maps, and microtubule  
662 ends on directional movement of a localising mRNA. *eLife*, 3:e01596.
- 663 Steward, O., Farris, S., Pirbhoy, P. S., Darnell, J., and Driesche, S. J. V. (2015). Localization and local translation of  
664 *Arc/Arg3.1* mRNA at synapses: some observations and paradoxes. *Front. Mol. Neurosci.*, 7.
- 665 Steward, O., Wallace, C., Lyford, G., and Worley, P. (1998). Synaptic Activation Causes the mRNA for the IEG *Arc*  
666 to Localize Selectively near Activated Postsynaptic Sites on Dendrites. *Neuron*, 21(4):741–751.
- 667 Steward, O. and Worley, P. F. (2001). Selective Targeting of Newly Synthesized *Arc* mRNA to Active Synapses  
668 Requires NMDA Receptor Activation. *Neuron*, 30(1):227–240.
- 669 Sutton, M. A. and Schuman, E. M. (2006). Dendritic protein synthesis, synaptic plasticity, and memory. *Cell*,  
670 127(1):49–58
- 671 Tang, Y., Scott, D. A., Das, U., Edland, S. D., Radomski, K., Koo, E. H., and Roy, S. (2012). Early and selective  
672 impairments in axonal transport kinetics of synaptic cargoes induced by soluble amyloid  $\beta$ -protein oligomers.  
673 *Traffic*, 13(5):681–693.
- 674 Verbrugge, S., van den Wildenberg, S. M., and Peterman, E. J. (2009). Novel Ways to Determine Kinesin-1's Run  
675 Length and Randomness Using Fluorescence Microscopy. *Biophys. J.*, 97(8):2287–2294.
- 676 Vickers, C. A., Dickson, K. S., and Wyllie, D. J. A. (2005). Induction and maintenance of late-phase long-term  
677 potentiation in isolated dendrites of rat hippocampal CA1 pyramidal neurones. *J. Physiol.*, 568(3):803–813.
- 678 Wang, X. and Schwarz, T. L. (2009). The Mechanism of  $Ca^{2+}$ -Dependent Regulation of Kinesin-Mediated  
679 Mitochondrial Motility. *Cell*, 136(1):163–174.
- 680 Welte, M. A. (2004). Bidirectional transport along microtubules. *Curr. Biol.*, 14(13):R525–R537.
- 681 Williams, A. H. (2016). PyNeuron Toolbox. <https://github.com/ahwillia/PyNeuron-Toolbox>.
- 682 Wong, R. O. and Ghosh, A. (2002). Activity-dependent regulation of dendritic growth and patterning. *Nat. Rev. Neurosci.*, 3(10):803–812.
- 684 Zagrebelsky, M. and Korte, M. (2014). Form follows function: BDNF and its involvement in sculpting the function

- 685 and structure of synapses. *Neuropharmacol.*, 76:628–638.
- 686 Zheng, N., Jeyifous, O., Munro, C., Montgomery, J. M., and Green, W. N. (2015). Synaptic activity regulates AMPA  
687 receptor trafficking through different recycling pathways. *eLife*, 4.